

# Unsteady Rotor Hub Passage Vortex Behavior in the Presence of Purge Flow in an Axial Low Pressure Turbine

**P. Jenny<sup>1</sup>**

e-mail: jenny@lec.mavt.ethz.ch

**R. S. Abhari**

Laboratory for Energy Conversion,  
Department of Mechanical  
and Process Engineering,  
ETH Zurich,  
8092 Zurich, Switzerland

**M. G. Rose**

Institute of Aeronautical Propulsion,  
University of Stuttgart,  
70569 Stuttgart, Germany

**M. Brettschneider**

**K. Engel**

**J. Gier**

MTU Aero Engines GmbH,  
Dachauer Strasse 665,  
80995 Munich, Germany

*The paper presents an experimental and computational study of the unsteady behavior of the rotor hub passage vortex in an axial low-pressure turbine. Different flow structures are identified as having an effect on the size, strength, shape, position, and the unsteady behavior of the rotor hub passage vortex. The aim of the presented study is to analyze and quantify the sensitivities of the different flow structures and to investigate their combined effects on the rotor hub passage vortex. Particular attention is paid to the effect of the rim seal purge flow and of the unsteady blade row interaction. The rotor under investigation has nonaxisymmetric end walls on both hub and shroud and is tested at three different rim seal purge flow injection rates. The rotor has separated pressure sides at the operating point under investigation. The nondimensional parameters of the tested turbine match real engine conditions. The 2-sensor fast response aerodynamic probe (FRAP) technique and the fast response entropy probe (FENT) systems developed by ETH Zurich are used in this experimental campaign. Time-resolved measurements of the unsteady pressure, temperature and entropy fields between the rotor and stator blade rows are taken and analyzed. Furthermore, the results of URANS simulations are compared to the measurements and the computations are also used to detail the flow field. The experimental results show a 30% increase of the maximum unsteadiness and a 4% increase of the loss in the hub passage vortex per percent of injected rim seal cooling flow. Compared to a free stream particle, the rim seal purge flow was found to do 60% less work on the rotor. [DOI: 10.1115/1.4007837]*

## Introduction

In gas turbine applications bypassed compressor air is injected through the rim seals between the stationary and rotating parts in order to prevent the ingestion of hot gases into the disk cavities. This is necessary to avoid the disk's overheating and thermal fatigue. The ingestion of hot gases is driven by disk pumping and the external nonuniform static pressure field. The secondary cooling mass flow considered for this work is the purge flow injected at the rim seal between the nozzle guide vane and rotor.

Kobayashi et al. [1] found experimentally that the minimum required cooling air flow rate is underestimated by the pressure difference criterion and that it is insensitive to rotational speed. Chew et al. [2] and Dadkhah et al. [3] studied the minimum required coolant flow in the context of different rim seal shapes and compared the results to the differential pressure criterion. The strong interaction between the injected cooling air and the secondary flow structures has been reported in the open literature. McLean et al. [4] experimentally tested "radial, impingement and root injection" cooling configurations as defined in [4]. They found that the cooling mass flow significantly affects the three-dimensional secondary flow structures and turbine stage performance. Ong et al. [5] reported a reduction of the efficiency penalty caused by the coolant flow when a swirl component is introduced to the coolant jet. Furthermore, they found that most of the coolant mass flow is entrained by the downstream blade hub secondary flows.

Experimental work in a transonic high pressure turbine conducted by Paniagua et al. [6] showed that the hub end wall cavity flow intensifies the rotor hub passage vortex and enhances its radial migration. Reid et al. [7] quantified the performance penalty caused by the hub rim sealing flow as being approximately 0.6% per percent of injected rim seal cooling mass flow. Marini and Girgis [8] investigated the effect of the blade leading edge platform numerically. They presented a design offering a 0.07% stage efficiency benefit and a reduced sensitivity to an increasing cavity mass flow. Schuepbach et al. [9] have investigated the sensitivity of efficiency to coolant purge flow in the presence of end wall profiling. Depending on the end wall design they reported a 0.7%–1.2% efficiency drop per percent of purge flow. Additionally, intensification and higher penetration of the hub secondary flows at the exit of the rotor under the effect of purge flow were observed.

The unsteady interaction mechanisms between secondary flows at rotor inlet and outlet have been investigated in detail by different researchers, such as Binder et al. [10] and Chaluvadi et al. [11]. Matsunuma [12] reported an intensive interaction between nozzle and rotor flow due to the rotating potential field of the rotor. Kasper et al. [13] undertook a three-dimensional visualization of the vortex instability at rotor inlet. They reported the vortex as breaking down in a spiral mode due to the blade row interaction.

This paper experimentally studies the unsteady effect of different levels of rim seal purge flow on the rotor hub secondary flows in the presence of a stationary blade row downstream of the rotor. An attempt to quantify the additional loss created by the purge flow in the hub loss core is proposed. Furthermore, two mechanisms causing the purge loss are investigated and quantified. The time-resolved measurements are taken in a rotating model shrouded low pressure axial turbine and compared to the results of corresponding URANS simulations.

<sup>1</sup>Corresponding author.

Contributed by the International Gas Turbine Institute (IGTI) of ASME for publication in the JOURNAL OF TURBOMACHINERY. Manuscript received August 7, 2012; final manuscript received August 31, 2012; published online June 28, 2013. Editor: David Wisler.

**Table 1 Operating conditions and geometrical characteristics**

$\Pi_{1.5}$	$1.65 \pm 0.4\%$ (–)
$T_{t,in}$	$328 \pm 0.2$ (K)
$\dot{m} \sqrt{T_{t,in}}$	$152 \pm 0.2\%$ $\left[ \frac{\text{kg} \sqrt{\text{K}}}{\text{s} \times \text{bar}} \right]$
$\frac{P_{t,in}}{P}$	$2.48 \pm 0.05$ $\left[ \frac{r.p.s.}{\sqrt{\text{K}}} \right]$
$\sqrt{T_{t,in}}$	
Mach (NGV1 <sub>ex</sub> /R1 <sub>ex</sub> /NGV2 <sub>ex</sub> )	0.52/0.53/0.48 (–)
Re (NGV1/R1/NGV2)	$7.1/3.8/5.1 \cdot 10^5$ (–)
Blade count (NGV1/R1/NGV2)	36/54/36 (–)
Aspect ratio (NGV1/R1/NGV2)	0.87/1.17/0.82 (–)

## Experimental Method

The experimental investigation was performed in the “LISA” research turbine at the Laboratory for Energy Conversion at the Swiss Federal Institute of Technology (ETH).

**Experimental Turbine Facility.** The air-loop of the facility is quasi-closed and includes a radial compressor, a two-stage water to air heat exchanger, and a calibrated venturi nozzle for mass flow measurements. Upstream of the 1.5 stage turbine section is a 3 m flow conditioning stretch to ensure a homogenous flow field. Additionally, the flow undergoes acceleration before the turbine section in order to reduce the significance of remaining flow non-uniformities from upstream. At the exit of the turbine section the air loop opens to the atmosphere. A dc generator absorbs the turbine power and controls the rotational speed with an accuracy of  $\pm 0.02\%$  ( $\pm 0.5$  rpm). A heat exchanger controls the inlet total temperature  $T_{t,in}$  to an accuracy of  $\pm 0.3\%$ . A torque meter measures the torque on the rotor shaft. The nozzle guide vane and the shrouded rotor have shaped end walls. The main features and the methodology of the corresponding end wall design can be found in Jenny et al. [14]. The rotor has end wall profiling on the hub and shroud and its airfoils are partially representative of a low pressure turbine.

**Operating Conditions.** During all measurements the turbine 1.5 stage total-to-static pressure ratio is kept constant at  $\Pi_{1.5} = 1.65$  and the total turbine entry temperature is kept uniform at  $T_{t,in} = 328$  K. The operating conditions and geometrical characteristics are detailed in Table 1. In order to account for the change in ambient pressure on different measurement days, the measured pressures are nondimensionalized by the respective inlet total pressure. These operating conditions permit an accurate comparison between measurements made on different days.

**Injection System.** The air injected through the rim seal between the nozzle guide vane and rotor is bled off the primary air-loop upstream of the main flow conditioning stretch. The mass flow of the bypassed air ( $\dot{m}_{bypass}$ ) is measured by means of a venturi, which is part of the auxiliary air system. After having passed a plenum, the air is fed into the rim seal cavity through tunnels inside the first nozzle guide vanes. Figure 1 illustrates the leakage path and the rim seal cavity. From the cavity underneath the nozzle guide vanes there are two leakage paths, which are indicated in Fig. 1 as dotted arrows. One path is through the upstream rim seal into the main flow,  $\dot{m}_{purge}$ . The rest of the gas ( $\dot{m}_{drum}$ ) is ejected through the drum to ambient conditions after being measured in another venturi. The pressure difference over the labyrinth seal between the downstream rim seal and the drum is balanced. Under these conditions the net mass flow through the downstream rim seal into the drum is assumed to be zero. Thus the injected purge mass flow can be calculated as the difference between the measured bypass and the drum mass flow. The injection rate (IR) is defined as the ratio between the injected mass flow and the total turbine mass flow, given by Eq. (1),

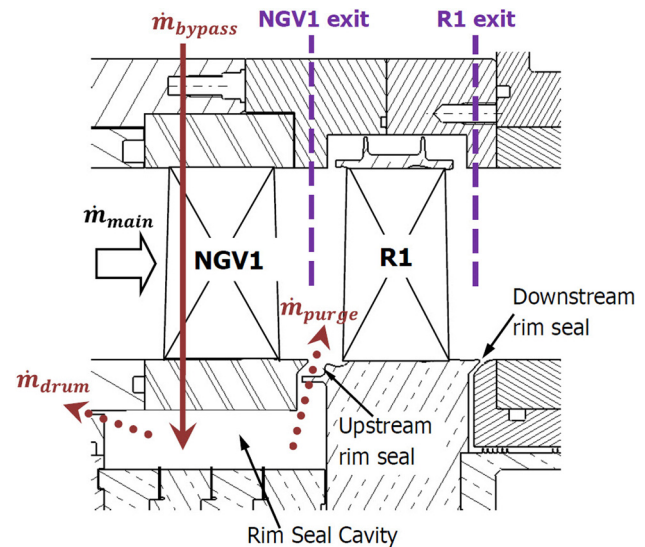


**Fig. 1 Illustration of leakage path and NGV1 exit and rotor exit measurement planes**

$$IR = \frac{\dot{m}_{purge}}{\dot{m}_{main}} = \frac{\dot{m}_{bypass} - \dot{m}_{drum}}{\dot{m}_{main}} \quad (1)$$

The measurements were conducted with the following three different injection rates: IR = 0.4%, 0.8%, 1.2%, which are representative of low, nominal and high injection rates.

**Measurement Planes.** The data were measured at two different traversing planes in the turbine test facility. Figure 1 shows the blade rows and relative positions of the two traverse planes at the NGV1 exit and rotor exit. At these traverse planes the spatial resolution of the measurement grid consisted of 39 radial and 41 equally spaced points in the circumferential direction covering one stator pitch. The measurement grid shows radial clustering near the end walls.

**Measurement Technology.** The unsteady turbine flow field was measured using a standard fast response aerodynamic probe (FRAP) and the fast response entropy probe (FENT), both developed at the Laboratory for Energy Conversion at the ETH Zurich. The FRAP (Kupferschmied et al. [15] and Pfau et al. [16]) is capable of capturing unsteady flow features up to frequencies of 48 kHz based on measurements including total and static pressures, flow yaw and pitch angles, and Mach number. The standard FRAP has a 1.8 mm tip diameter and is equipped with two sensors. The probe is operated in a virtual 4-sensor mode to measure three-dimensional, time-resolved flow properties. Table 2 gives the relative measurement uncertainties of the FRAP as a percentage of the calibration range of  $\pm 30$  deg for the yaw angle,  $\pm 20$  deg for the pitch angle, and as a percentage of the dynamic head for the total and static pressure.

The time-resolved temperature measurements were carried out with the FENT probe designed and developed by Mansour et al. [17]. The probe has a diameter of 1.8 mm and a measurement bandwidth of 48 kHz. It consists of two parts: first, a miniature silicon piezo-resistive chip is glued beneath a pressure tap to measure the unsteady static and total pressures, and secondly, a pair of

**Table 2 Relative uncertainty of the FRAP**

Yaw angle	Pitch angle	$P_t$	$P_s$
0.8%	2.3%	1.0%	1.2%

**Table 3 Relative uncertainty of the FENT probe**

$P_t$	$T_t$	$\Delta s$
0.1%	2.5%	2.51%

thin film gauges with a thickness of about 200 nm are operated as resistance thermometers at two different film temperatures and used to measure the unsteady total temperature. The absolute uncertainties in the measurements and derived quantities are summarized in Table 3. Knowing unsteady temperature and pressure, the unsteady relative entropy can be calculated. Due to geometrical constraints the unsteady temperature and pressure are measured at different locations on the same probe. Therefore, a corresponding measurement grid is used that allows the data to be shifted in the radial direction by the distance between the pressure measurement hole and the thin film gauges during postprocessing. As a consequence, both signals are from the same location before the entropy is calculated.

For both probe measurement techniques the data are acquired at a sampling rate of 200 kHz over a period of 2 s. The postprocessing is done for three consecutive rotor pitches. The sampling rate resolves 82 points per rotor pitch. During these 2 s the three blade passing events are phase-lock-averaged 85 times.

### Time-Resolved Computational Model

**Grid and Boundary Conditions.** The grid used for the time-resolved simulations is structured and has a total of  $18.5 \times 10^6$  nodes. As the blade count ratio between stationary and rotating blade rows is 2–3, two vane passages of the first and second vane rows and three rotor passages are represented in the mesh with periodic boundary conditions in the circumferential direction. In order to have a realistic rim seal flow field the cavity space between rotor disk and first vane row is fully modeled. The nondimensionalized wall distances on the airfoils and the end walls are on average  $y^+ = 1.5$ . At the inlet of the turbine domain a constant total pressure and total temperature corresponding to the measured experimental operating conditions were applied. At the exit the measured mass flow at these inlet conditions was imposed as a boundary condition. The purge mass flow rate, measured static pressure, and temperature were imposed as boundary conditions at the rim seal cavity inlet.

**Solver.** The time-resolved results were achieved with the commercial ANSYS CFX Version 12.1 software package. The temporal resolution is 80 time steps per period, corresponding to three rotor blade passing events. The shear stress transport (SST) turbulence model without transition modeling was used for the simulations. The maximum residuals were found to be in the order of  $10^{-3}$ , while the mass imbalances were in the order of  $10^{-5}$ . The periodic convergence of the unsteady simulations was judged based on a correlation coefficient over 99% of two pressure monitoring points at the rotor exit and typically reached after 25 periods.

**Validation.** The time-averaged results of the unsteady CFD calculation are compared to the experimental results in order to validate the computational model used for the simulations. The validation is done for all the experimentally investigated injection rates. As an example, Fig. 2 shows the comparison between the measurement and the numerical prediction of the circumferentially mass and time-averaged radial distribution of the flow angle at the rotor exit for the nominal injection rate of  $IR = 0.8\%$ . Five-hole probe and FRAP measurements are compared to the numerical prediction in Fig. 2. Below 90% span the absolute difference in flow yaw angle is between  $-2$  deg and  $4$  deg for the FRAP and  $\pm 4$  deg for the 5-hole probe. The radially averaged

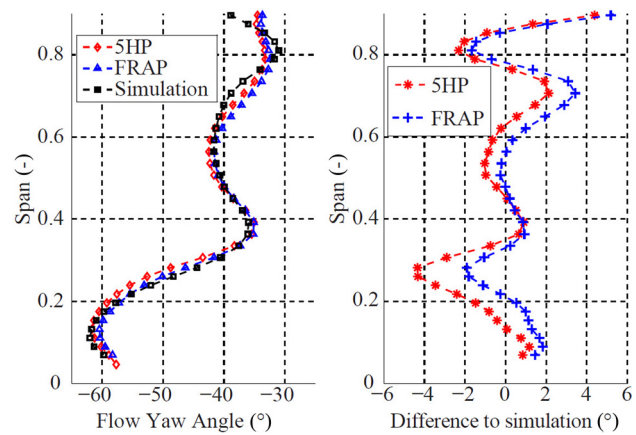


**Fig. 2 Comparison between measured and simulated relative flow yaw angle at the rotor exit for the nominal injection rate ( $IR = 0.8\%$ )**

difference in flow yaw angle is approximately  $-1$  deg for the 5-hole probe and  $-0.5$  deg for the FRAP. Compared to the measurements of both probe types, the radial position, shape and strength of the hub loss core are well predicted by the numerical simulation. A more detailed comparison between the numerical simulation and the measurements can be found in [14].

**Particle Tracking.** In order to get a more detailed view of the rotor hub loss core flow field, an in-house particle tracking post-processing tool was developed. The flow field velocity field is written out by the solver at each time step and then used as an input for the particle tracking tool. The time marching of the particles is based on the third order Adams–Bashforth method [18] with four subiterations. This postprocessing tool computes the three-dimensional track of massless particles based on the actual location and the velocity field at the current and the two former time steps. The particle tracker is used in the forward and backward time mode.

### Results and Discussion

In the first part of the following section the unsteady behavior of the rotor hub loss core under the effect of three different injection rates is studied based on FRAP measurements. In the second part, an approach is proposed to quantify the additional loss in the hub passage vortex due to the increased purge flow rate. Time-resolved FENT probe measurements are studied in this part. Corresponding CFD simulations in the third part continue the analysis by providing information on the rotor intrarow flow field. A backtracking algorithm is used for particles released inside the hub loss core at the rotor exit in order to define their path and origin.

**Interaction Mechanisms Between Purge Flow and Rotor Hub Passage Vortex.** Previous experimental investigations (Schuepbach et al. [19], Ong et al. [5]) have shown that the purge flow strongly interacts with the rotor hub passage vortex. It becomes more unsteady and tends to radially migrate under the effect of increased rim seal purge flow. Jenny et al. [14] reported a 10% radial migration and a 30% increase in maximum measured unsteadiness per percent of injected purge flow for the turbine configuration under investigation.

Figure 3 shows the radial distribution of circumferentially mass and time-averaged measured nondimensionalized streamwise vorticity  $\Omega_s$  at the rotor exit for the three tested injection rates. The time-resolved streamwise vorticity was calculated as the scalar product of the vorticity vector and the primary flow vector. The required axial gradients are approximated using a frozen flow

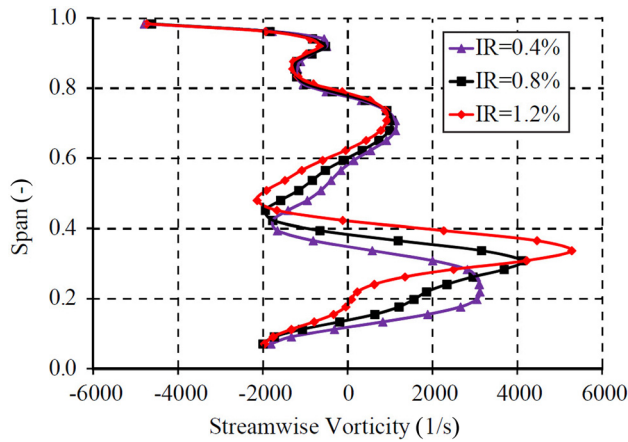


**Fig. 3 Radial distribution of circumferentially mass and time-averaged nondimensionalized streamwise vorticity  $\Omega_s$  (1/s) for the three investigated injection rates**

structure assumption. The detailed approach and the corresponding calculation method can be found in Schuepbach et al. [20]. The circumferentially mass and time-averaged distribution of  $\Omega_s$  for the high injection rate shows a concentration of high streamwise vorticity flow at a limited spanwise region compared to the low injection rate. Flow with high streamwise vorticity seems to become concentrated at a higher spanwise position for the high injection rate. Figure 3 confirms the radial migration of the hub loss core as a consequence of increased injection rate. Assuming the center of the hub loss core to be at the spanwise position of maximum streamwise vorticity, the vortex radially migrates outwards by 12% absolute spanwise position per percent of injected purge flow. For the following analysis the center of the hub loss core is assumed to be at approximately 35% span at the high injection rate and at 23% span at the low injection rate.

Figure 4 shows the corresponding time-averaged contour plots of  $\Omega_s$  at the rotor exit in the rotor frame of reference for the high and low injection rates. Under the effect of increased purge flow the high vorticity flow not only concentrates at a higher spanwise position, but also tends to be stretched in the circumferential direction. The circulation of the hub loss core has been calculated as an area integral of  $\Omega_s$  inside an isocontour of zero streamwise vorticity. The calculated circulation based on the time-averaged streamwise vorticity increases by approximately 10% per percent of injected fluid. The area covered by the hub passage vortex (inside the isocontour of zero streamwise vorticity) increases by the same amount. The measured peak streamwise vorticity in the

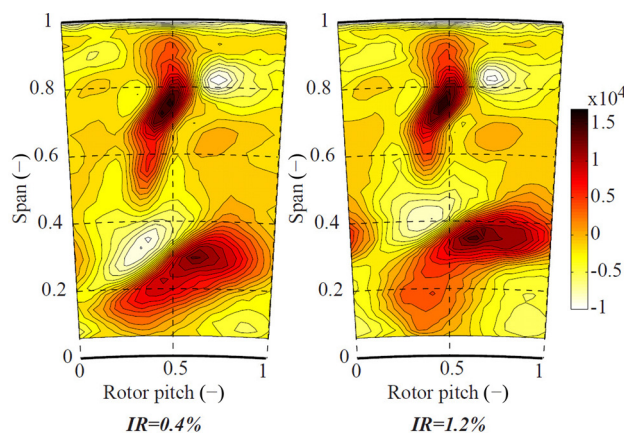


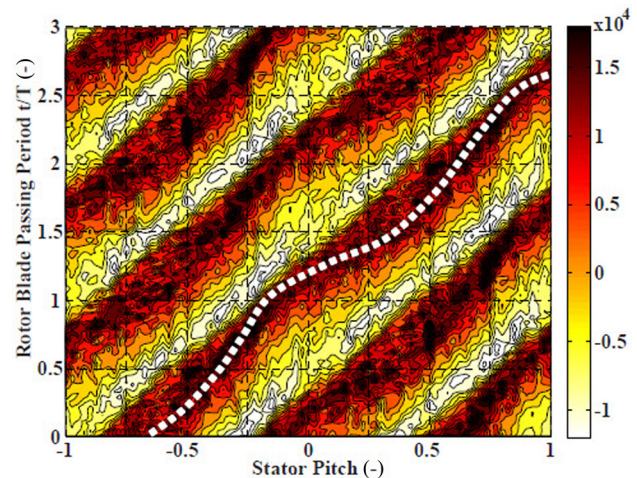
**Fig. 4 Time-averaged area plot in rotor relative frame of reference at the rotor exit. The parameter is the nondimensionalized streamwise vorticity  $\Omega_s$  (1/s) at low and high injection rates.**

hub loss core also increases by approximately 10% per percent of injected purge flow. In comparison, the purge flow causes the measured level of nondeterministic unsteadiness to increase more significantly by causing additional turbulence.

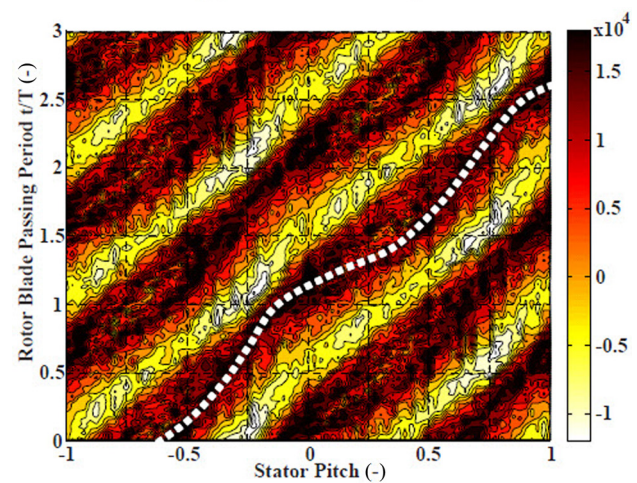
Figure 5 shows two time space plots of the nondimensionalized streamwise vorticity  $\Omega_s$  at the rotor exit for low and high injection rates. The radial position of the two plots was chosen not to be identical in order to take into account the radial migration of the hub passage vortex under the effect of purge flow. Both plots are produced at the height of the nominal center line of the hub loss core.

The inclined high  $\Omega_s$  features are the signature of the rotor hub passage vortex, a moving flow element in the stationary frame of reference. The gradient of the inclined high  $\Omega_s$  feature in the time space plot corresponds to the circumferential velocity of the hub passage vortex.

A steeper gradient corresponds to slower circumferential velocity (less distance per time). The dotted lines in Fig. 5 represent the approximate center of the hub loss core at a fixed radial position. For both injection rates the dotted lines have a kink per stator pitch and on either side of the kink the gradient is different. Therefore, the circumferential velocity of the hub passage vortex is not constant. This effect must be due to the presence of the static pressure field of the downstream vane. The effect occurs for every rotor hub passage vortex at the same circumferential position in



(a)  $IR = 0.4\%$  at 27% span.



(b)  $IR = 1.2\%$  at 35% span.

**Fig. 5 Time space plot in absolute frame of reference of the nondimensionalized streamwise vorticity  $\Omega_s$  (1/s) for low and high injection rates at the rotor exit**

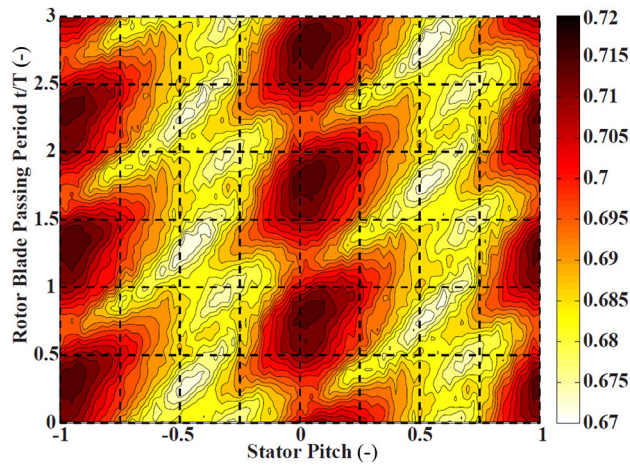
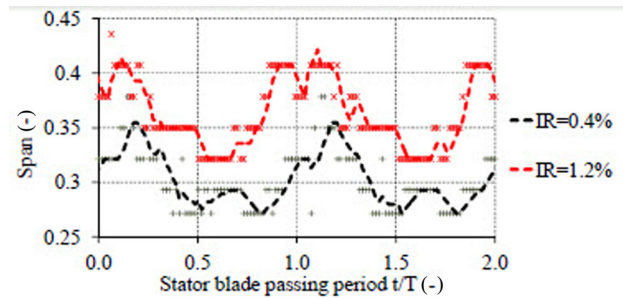


Fig. 6 Time space plot in absolute frame of reference of the normalized static pressure (-) at the rotor exit (IR = 1.2% at 35% span)

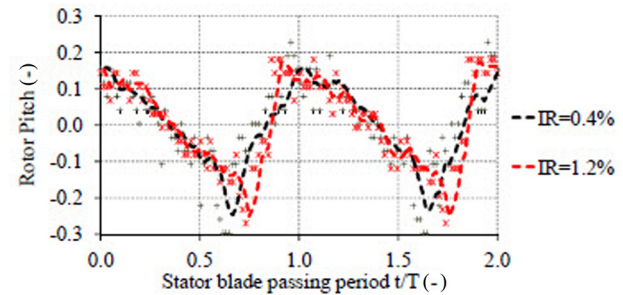
Fig. 5. The circumferential position of the NGV2 leading edge can be defined with the corresponding time space plot of static pressure shown in Fig. 6. The vertically stacked patches of high static pressure at around  $-0.95$  and  $0.05$  stator pitch in Fig. 6 are the signature of two neighboring leading edges of the second nozzle guide vane, a stationary feature with regard to space. The temporal variation of the static pressure potential field of the NGV2 leading edge is caused by the interaction with the passing rotor wakes; there is one trough per passing rotor wake and loss core.

The comparison of Figs. 6 and 5 reveals that the circumferential velocity of the hub passage vortex peaks just in front of the second guide vane leading edge, just where the static pressure field also peaks. When the hub passage vortex is approaching the increased static pressure zone of the NGV2 leading edge, it first slows, but then quickly flips to the other side at high circumferential velocity and finally continues at blade speed. When passing the static pressure potential field of the second nozzle guide vane the hub loss core is being forced to stretch. As a consequence, it has to speed up and spin faster. The static pressure at the core drops and its kinetic energy increases, creating additional friction loss with the surrounding flow. The more the vortex is stretched, the faster it spins and the more loss is created at its core. Such a flow situation will also tend to locally bend and diffuse the vortex. These things are both classically understood to lead to vortex breakdown. In Fig. 5 the diagonal track of the hub passage vortex can be seen to adopt a bifurcated form: this occurs for example at about  $(-0.9, 0.6)$  and  $(0.1, 2.25)$ . While it is not readily apparent why this is so, there is some similarity to the spiral vortex breakdown mode reported by Kasper et al. [13]. However in this reference a NGV wake was studied at the rotor inlet, whereas here a rotor hub passage vortex entering the second nozzle guide vane is analyzed. The swirl ratio of the vortex is below 0.25 and the unsteady measurements show no flow reversal.

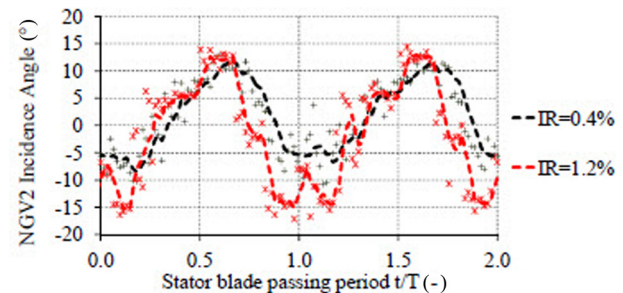
Figures 7(a) and 7(b) show the radial and circumferential position of the maximum experimental rms in the hub passage vortex in the rotor frame of reference at the rotor exit for low and high injection rates. The time dimension on the x-axis covers two stator blade passing events. The two figures show that the hub loss core is radially and circumferentially moving in the rotor frame of reference due to the blade row interaction. The radial migration of the hub loss core due to increased purge flow rate is confirmed in Fig. 7(a), when the average of the two curves is compared. This also shows that the spanwise range covered by the loss core during one period is not significantly influenced by the injection rate. The hub passage vortex travels approximately 10% in the radial dimension from peak to peak during one period for both injection



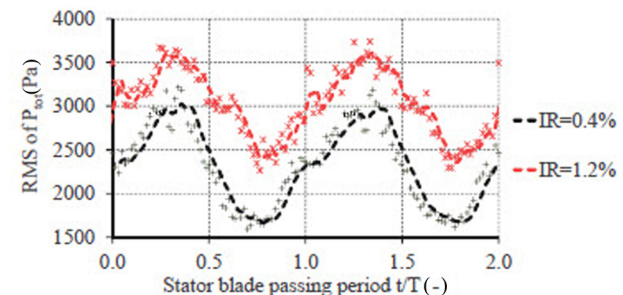
(a) Radial position of maximum rms of the relative total pressure signal in the hub passage vortex.



(b) Relative circumferential position of maximum rms of the relative total pressure signal in the hub passage vortex.



(c) NGV2 incidence at the center of hub passage vortex.



(d) Maximum rms of relative total pressure at the center of hub passage vortex.

Fig. 7 Unsteady spatial behavior of hub loss core at the rotor exit for minimum and maximum injection rates

rates. However, there appears to be a temporal phase shift between the two injection rates. At the high injection rate the hub passage vortex starts the radial migration 0.2 periods earlier compared to the low injection rate.

Figure 7(b) shows how the relative circumferential position of the hub passage vortex within the rotor is changing during the period cycle due to the blade row interaction. The circumferential range is large, at approximately 40% rotor pitch, and is unaffected by the purge flow rate. The shape of the curves in Fig. 7(b) is broadly a zig-zag with a slow fall and a quick rise. The event associated with the quick rise is when the high pressure of the NGV leading edge goes by. The purge flow intensity changes the rate of

rise of the curves in Fig. 7(b), but does not influence the slow fall. Apparently the structure of the hub passage vortex, influenced by the strong purge flow, moves circumferentially more rapidly past the NGV2 leading edge potential field at the high injection rate.

When combining Figs. 7(a) and 7(b) an unsteady two-dimensional movement of the hub passage vortex due to the blade row interaction can be derived. When the hub passage vortex is forced by the rotor to pass in front of the NGV2 leading edge potential field its radial position increases. The opposite mechanism occurs when the hub passage vortex is between two NGV2 leading edge potential fields.

The mechanism described causes the incidence of the hub passage vortex flow on the NGV2 to fluctuate unsteadily. Figure 7(c) shows the measured unsteady incidence on the NGV2 at the positions of the hub passage vortex defined in Figs. 7(a) and 7(b). Comparing the measurements at low and high injection rates, the maximum negative incidence on the NGV2 is decreasing by 10 deg and the maximum positive incidence is increasing by 2 deg. The range of incidence between minimum and maximum increases by about 15 deg per percent of injected purge flow. This additional positive and negative incidence can be expected to increase the loss at the NGV2 for the higher injection rate. The incidence variation is slightly influenced by the radial migration of the hub loss core. The NGV2 has only a 1 deg variation in inlet angle over the 10% height range of the vortex motion (Fig. 7(a)).

Figure 7(d) shows the nondimensionalized maximum rms value measured at the positions of the hub passage vortex defined in Figs. 7(a) and 7(b). The higher overall rms level at the high injection rate is as expected and has already been described. The variation of the rms signature of the rotor hub passage vortex is broadly a symmetrical zig-zag, Fig. 7(d). The minimum of the rms values occurs just as the pressure starts to rise due to the downstream leading edge and is almost unaffected by the purge flow rate. The rms level rapidly increases as the hub passage vortex wraps around the NGV2 leading edge. This effect is stronger with less purge flow and weaker with more. While the hub passage vortex rms is elevated by the purge flow, the variation in rms over the vane passing cycle is diminished.

**Measured Loss in Hub Passage Vortex.** In the next section, the additional loss caused by the increased purge flow injection rate is studied and an approach to quantify this loss is proposed. The variable chosen for the analysis is the experimental unsteady isentropic efficiency  $\eta_{is}$  at the rotor exit. Isentropic efficiency is a nondimensional number that directly compares the actual work to the ideal work for each fluid particle. When  $\eta_{is}$  is used, two assumptions need to be made: The flow is adiabatic and all the fluid has the same initial conditions. The isentropic efficiency could be artificially increased assuming heat loss in the turbine stage. The actual work would appear to be greater because there is a higher enthalpy change due to this heat loss. The heat loss in the test rig cannot be quantified exactly, but can be assumed to be similar during the measurements at all different injection rates, which allows for relative comparisons. The FENT probe measurements include unsteady total pressure and temperature. Hence, the unsteady isentropic efficiency can be calculated based on the FENT measurements using the local definition in the following equation:

$$\eta_{is} = \frac{1 - \frac{T_{tot,ex}}{T_{tot,in}}}{1 - \left(\frac{P_{tot,ex}}{P_{tot,in}}\right)^{\frac{\gamma-1}{\gamma}}} \quad (2)$$

Figure 8 shows the mass and time-averaged radial distributions of  $\eta_{is}$  for the three investigated injection rates. The corresponding area plots in the rotor frame of reference are shown in Fig. 9. The deficit of  $\eta_{is}$  present on the radial mass and time-averaged

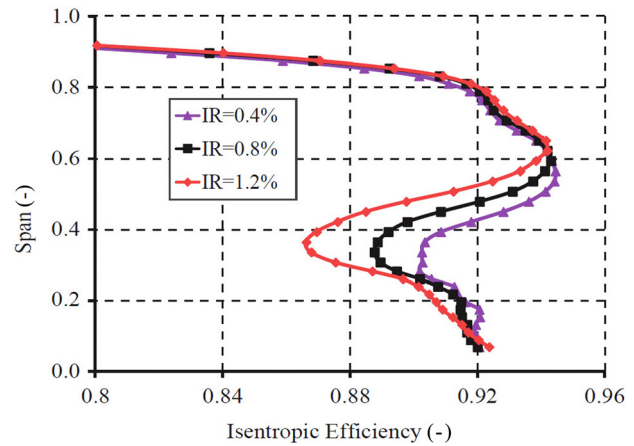


Fig. 8 Radial distribution of circumferentially mass and time-averaged isentropic efficiency  $\eta_{is}$  (-) at the rotor exit for the three injection rates investigated

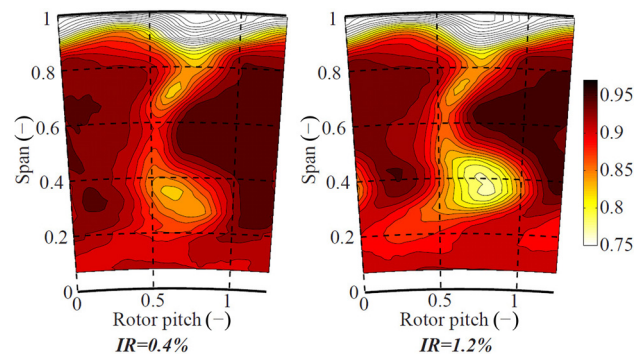
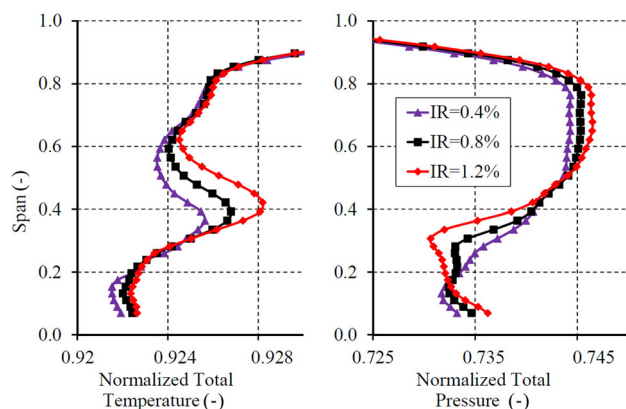


Fig. 9 Time-averaged area plot in rotor relative frame of reference at the rotor exit. The parameter is isentropic efficiency (-) at low and high injection rates.

distributions between 20% and 60% span is caused by the additional loss inside the hub passage vortex. The rest of the flow field appears to be much less affected by the different levels of purge flow. In order to quantify the significance of the lower efficiency in the hub passage vortex compared to the efficiency of the whole machine, a mass weighted average over one entire rotor pitch is calculated. This mass weighted  $\eta_{is}$  decreases by 1.5% per percent of injected purge flow, whereas a mass-averaged integral of the isentropic efficiency in the hub loss core decreases by 4% per percent of injected purge flow. Jenny et al. [14] reported a total-to-total efficiency decrease of 1.3% per percent of injection rate when considering a machine efficiency definition taking into account the effect of the rim seal purge flow at the inlet.

Figure 10 shows the mass and time-averaged radial distributions of total pressure and total temperature, the two variables required to calculate  $\eta_{is}$ . It is interesting to note that the effect of the purge flow on the total temperature is significant at higher radius (between 40% and 60% span), while the effect of the total pressure is at lower radius (between 20% and 40% span). Assuming the center of the vortex to be at 23% for the low and at 35% for the high injection rate as defined in Fig. 3, the purge flow causes the temperature to mainly increase in the top part of the vortex and the total pressure to mainly decrease in the lower part of the vortex. The proposed mechanism that causes the total temperature to rise in the top of the vortex is radial migration. At constant rothalpy the total temperature varies with the Euler work group  $UV_\theta$ . The blade speed  $U$  increases when the flow radially migrates outwards. Provided that the flow angle and relative Mach number do not significantly change, a radius increase of the flow



**Fig. 10 Radial distribution of circumferentially mass and time-averaged normalized total pressure and temperature at the rotor exit for the three investigated injection rates**

is a work reduction; hence  $T_{\text{tot}}$  increases. The additional purge flow causes radial migration of the hub passage vortex and therefore enforces the increase in the total temperature in the top part of the vortex.

The small difference in inlet temperature ( $-2$  K) between purge flow and free stream does not explain the changes in the top part of the vortex shown in Fig. 10. The slight increase in total pressure between 60% and 80% span (Fig. 10) causes the isentropic efficiency to slightly increase in this part of the flow field (Fig. 8). Reduced profile loss of the rotor is considered to be one of the reasons for this increase of  $P_{\text{tot}}$ . Due to the additional purge flow, the rotor sees a slightly higher total to static pressure ratio, which increases the acceleration and hence reduces profile loss.

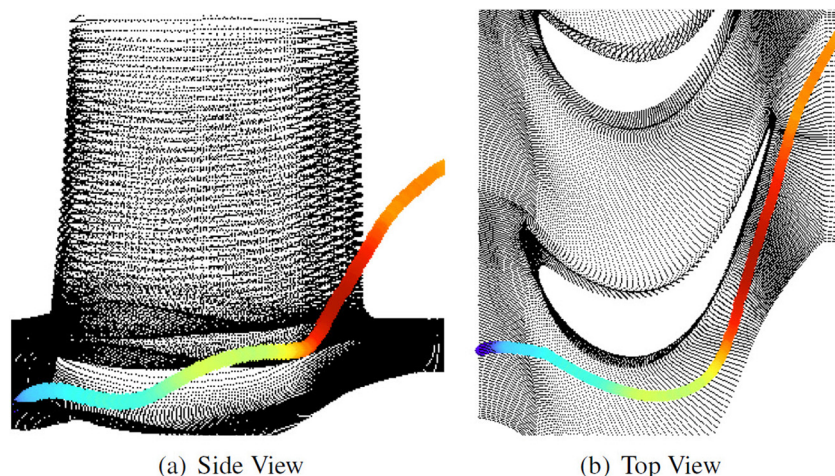
**Purge Losses: Lagrangian Perspective.** The numerical simulations performed in parallel to the measurements were used to detail the flow field in the rotor passage. Particles were released in the hub passage vortex at the rotor exit and tracked in a backward time mode in order to see where they came from and which path they follow in the rotor flow field. Classically, the following fluid sources for the rotor hub passage vortex would be expected: rotor end wall boundary layer, radially migrating fluid on the rotor suction side, purge flow out of the rim seal cavity, NGV hub end wall boundary layer, NGV wakes, and hub loss core. For the operating point under investigation, the turbine rotor blades have pressure side separations. Jenny et al. [14] have shown that the fluid inside

the pressure side bubble leaves the rotor blade row inside the hub passage vortex. The fluid from the listed sources has lower relative momentum than the free stream flow and therefore migrates to the regions of low reduced static pressure in the rotor flow field. The reduced static pressure is known from literature (Moore [21], Greitzer et al. [22]). Generally speaking, low relative momentum flow from the listed sources migrates radially inwards and towards the suction side of the rotor where it interacts with the rotor hub passage vortex. Many of the listed sources include highly complex flow interaction mechanisms and will not be included in this paper. Typical particle tracks of particles leaving the rim seal cavity will be presented and studied.

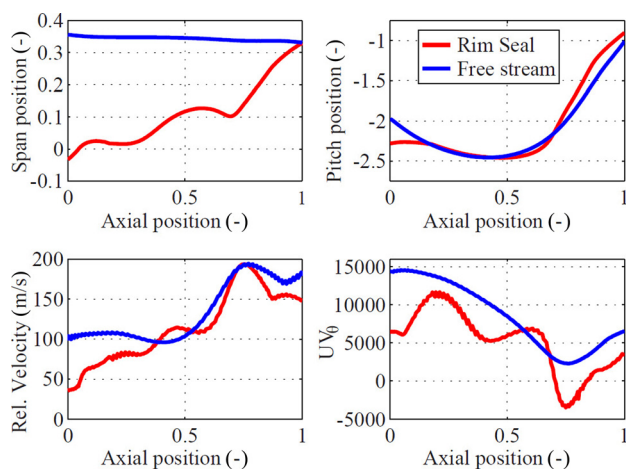
Two injection strategies for the backward tracking of the particles were considered. As a first option, particles were introduced at a different position at each time step in function of the unsteady spatial movement of the hub passage vortex that has been described (Fig. 7). Particles were injected during one period inside a circular cloud around the moving center of the hub loss core. The center of the cloud is defined using the maximum value of the Q-criterion (second invariant of the velocity gradient tensor) at each time step of the simulation. As a second option, the particles were released at the same coordinates at each time step during one period. Again the particles were released inside a circle whose center is determined by the minimum time-averaged relative total pressure in the hub passage vortex.

Figure 11 shows the top and side view of a typical particle track of a purge flow particle leaving the rim seal cavity seen in the relative frame. Figure 12 details radial position, circumferential position, relative velocity (kinetic energy), and the Euler work term in function of the nondimensionalized axial position of the particle track shown in Fig. 11. In comparison, Fig. 12 also shows the corresponding track details for a free stream particle leaving the rotor blade row at the same radial position as the particle leaving the rim seal cavity. When the particle leaves the rim seal cavity it has much lower rotor relative velocity compared to the particles leaving the nozzle guide vane.

The flow above the rim seal leaving the NGV at low span is expected to have the highest relative velocity. The relative velocity at the rim seal exit (radius equal to rotor hub radius) of the analyzed particle is approximately three times lower compared to the free stream particle, however at a higher radial position. The significant velocity mismatch at the exit of the rim seal cavity represents loss generation opportunities. It is therefore considered to be one of the reasons for the increased loss and turbulence in the passage vortex, especially at the high injection rate. When the particle has left the cavity it is strongly accelerated and starts to interact with the hub passage vortex. In the relative frame the



**Fig. 11 Top and side view of a typical particle track of particles leaving the rim seal cavity (IR = 0.8%) seen in the relative frame. The color of the particles indicates relative velocity.**



**Fig. 12 Position, relative velocity, and Euler work term of the particle presented in Fig. 11 and a free stream particle leaving the rotor blade row at the same radius. The parameters are plotted in function of the nondimensionalized axial position: 0 corresponds to the start of the particle at rotor inlet and 1 corresponds to the moment when the particle leaves the rotor domain.**

particle under investigation in Fig. 12 is accelerated by a factor of 5 from rotor inlet to rotor outlet. The increasing and decreasing spanwise position in Fig. 12 indicates a vortical motion during the radial migration of the particle. The particle has become part of the hub passage vortex. Figure 12 also shows that the particle leaving the rim seal cavity is accelerated in the circumferential direction in the early rotor passage. As the purge flow fluid enters the rotor it travels directly towards the low pressure of the suction side of the rotor. As it does so, the rotor does work on it with  $UV_\theta$  climbing from  $6000 \text{ m}^2/\text{s}^2$  to  $11000 \text{ m}^2/\text{s}^2$ , its stagnation enthalpy rises and the turbine rotor is locally a compressor. The purge flow particle almost attains the  $UV_\theta$  value of the free stream, but then enters the passage vortex, following an oscillatory path, Fig. 11. As the particle orbits the vortex it alternately gains and loses stagnation enthalpy.

When the purge flow particle joins the passage vortex it has a circumferential velocity typical of a free stream particle, but it is joining low momentum fluid. The velocity differences between the purge flow particle and the free stream can be expected to indicate shear stresses and viscous dissipation. The kinetic energy of the purge particle will be viscously destroyed and the entropy will rise. Thus the work processes acting on the purge fluid extract energy from the rotor, deliver it to the particle only to be dissipated viscously by friction. This suggests that work processes are a part of the loss mechanisms involved in the hub loss core. The difference in Euler work for the rim seal purge flow particle is approximately  $\Delta UV_\theta = 3000 \text{ m}^2/\text{s}^2$ . For the free stream particle the corresponding number is  $\Delta UV_\theta = 7500 \text{ m}^2/\text{s}^2$ . In other words, the purge flow particle only does about 40% of the work on the rotor compared to the free stream particle. Hence the purge flow fluid reduces the work of the turbine as well as causing additional mixing losses.

A typical flow path of particles leaving the rotor blade row inside the hub passage vortex originating from the pressure side bubble present at the chosen operating point has been described by Jenny et al. [14] using the same rotor. Under the effect of the reduced static pressure gradient the bubble fluid radially migrates towards the hub. Once the particles have arrived on the hub end wall, the cross passage gradient causes them to travel along the shaped end wall across the passage to the suction side. Once the pressure side bubble flow arrives on the suction side, it starts interacting with the suction side hub secondary flows. The strong acceleration of the bubble fluid inside the hub passage vortex

causes additional loss. The work process of a particle in the bubble is difficult to assess, because it has already done work on the rotor before it joined the pressure side separation and because its origin is difficult to define. The backwards particle tracking has been used in order to statistically define the percentages of the different flow sources of the hub passage vortex. Thus, for each test case five thousand particles were injected at the rotor exit inside the hub passage vortex using the injection methods described and backtracked to their origin. At a nominal injection rate approximately 15% of the particles in the hub passage vortex were found to originate from the rim seal cavity. The corresponding approximate percentages at low and high injection rates are 10% and 22%. This relatively small percentage of the hub passage vortex flow causes the 4% increase in loss and the 30% increase in experimental unsteadiness per percent of injected purge flow. Depending on the injection rate, the fluid leaving the pressure side separation was found to represent between 1% and 3% of the total hub passage vortex flow. As described by Jenny et al. [14], the pressure side bubble increases in size with increasing purge flow rate. Hence more flow leaves the pressure side bubble at higher injection rate via the described path. However, the effect of the purge flow on the measured unsteadiness in the hub loss core appears to be one order of magnitude stronger than the effect of the pressure side bubble. Approximately 40%–50% of the hub passage flow was detected to come from the rotor end wall and blade boundary layers. This number was only slightly affected by the amount of purge flow injected. A particle was considered as boundary layer flow when it was on average closer than 0.5 mm to the end wall on its track. The remaining percentage of the hub passage vortex flow is considered to originate from the NGV wakes, hub end wall boundary layer, and hub loss core.

## Conclusions

This paper presents the results of a combined experimental and computational investigation of the unsteady behavior of the hub passage vortex at the exit of a turbine rotor with separated pressure sides. The time-resolved measurements were made in a one-and-half stage shrouded model axial turbine with profiled NGV and rotor end walls using a fast response aerodynamic probe in combination with a fast response entropy probe. Three different levels of purge flow (0.4%, 0.8%, and 1.2%) were considered for the analysis.

The time-resolved measurements showed a highly unsteady movement of the hub loss core due to the blade row interaction. The core of the hub passage vortex was found to travel 10% span in the radial direction and 40% rotor pitch in the circumferential direction under the effect of the downstream stator blade passing event. These numbers are unaffected by the injection rate. However at a higher injection rate the hub loss core swings 30% more rapidly past the NGV2 leading edge potential field. At this injection rate, the hub loss core is transporting higher unsteadiness at lower static pressure. The unsteady movement of the hub passage vortex was found to locally increase the range of the incidence on the NGV2 between minimum and maximum by 15 deg per percent of injected purge flow, increasing the loss at the NGV2.

An attempt was made to quantify the additional loss created by the purge flow in the hub loss core. A time-averaged and mass-weighted integral of the unsteady isentropic efficiency in the hub loss core decreased by 4% per percent of injected purge flow. The total pressure and temperature distributions required for the calculation of the unsteady isentropic efficiency were provided by the FENT probe. The additional purge flow reduced the total pressure distribution in the lower half of the hub passage vortex and increased the total temperature distribution in the upper part of the vortex.

Based on the numerical simulations, particles were released inside the hub passage vortex at the rotor exit and tracked in a backward mode in order to define where they came from and which path they followed in the rotor flow field. Two potential

loss mechanisms were proposed for particles leaving the rim seal cavity. Firstly, the significant relative velocity mismatch near the rim seal between purge flow and free stream fluid is causing the loss to increase with increasing purge flow rate due to friction and viscous dissipation. Secondly, the rotor was found to do work on the rim seal purge flow in the early rotor passage by accelerating it in the circumferential direction. These work processes extract energy from the rotor and deliver it to the particle only to be dissipated viscously by friction in the hub loss core. The investigated purge flow particle was found to do 60% less work on the rotor compared to a free stream particle.

Based on a statistical approach, it was found that approximately 15% of the flow in the hub passage vortex is coming from the rim seal cavity at the nominal injection rate and is responsible for the 30% increase in measured nondeterministic unsteadiness per percent of injection rate. The effect of the flow from inside the pressure side separation on the rotor hub passage vortex unsteadiness was found to be an order of magnitude smaller, as it only represents 1%–3% of the flow in the hub passage vortex, depending on the amount of purge flow.

### Acknowledgment

The work leading to the results of this paper was carried out within the joint industrial and academic research program that is part of the “Luftfahrtforschungsprogramm LuFo4” supported by the German Federal Ministry of Economics and Technology. The authors wish to thank MTU Aero Engines for permission to publish this paper.

### Nomenclature

$\dot{m}$	= mass flow (kg/s)
$p$	= pressure (Pa)
$\bar{p}$	= time mean part of pressure signal (Pa)
$\tilde{p}$	= periodic part of pressure signal (Pa)
$p'$	= random part of pressure signal (Pa)
$T$	= temperature (K)
Re	= Reynolds number
IR	= injection rate (%)
$N$	= rotational speed (r.p.s.)
$t$	= time (s)
$V$	= velocity (m/s)
$U$	= rotational speed (m/s)
$\eta$	= efficiency
$\Pi$	= pressure ratio
$\gamma$	= isentropic coefficient
$\Omega$	= vorticity (1/s)

### Abbreviations

rms	= root mean square
NGV1	= first nozzle guide vane
NGV2	= second nozzle guide vane
R1	= rotor 1

### Subscripts

$t$	= stagnation flow quantity
$s$	= static flow quantity
rel	= relative frame flow quantity
red	= reduced
in	= turbine inlet flow quantity

$S$	= streamwise
$is$	= isentropic
$ex$	= blade row exit
$\theta$	= circumferential coordinate

### References

- [1] Kobayashi, N., Matsumoto, M., and Shizuya, M., 1984, “An Experimental Investigation of a Gas-Turbine Disk Cooling System,” *ASME J. Eng. Gas Turbines Power*, **106**(1), pp. 136–141.
- [2] Chew, J. W., Dadkhah, S., and Turner, A. B., 1992, “Rim Sealing of Rotor-Stator Wheelspaces in the Absence of External Flow,” *ASME J. Turbomach.*, **114**(2), pp. 433–438.
- [3] Dadkhah, S., Turner, A. B., and Chew, J. W., 1992, “Performance of Radial Clearance Rim Seals in Upstream and Downstream Rotor-Stator Wheelspaces,” *ASME J. Turbomach.*, **114**(2), pp. 439–445.
- [4] McLean, C., Camci, C., and Glezer, B., 2001, “Mainstream Aerodynamic Effects Due to Wheel-space Coolant Injection in a High-Pressure Turbine Stage: Part II—Aerodynamic Measurements in the Rotational Frame,” *ASME J. Turbomach.*, **123**(4), pp. 697–703.
- [5] Ong, J. H. P., Miller, R. J., and Uchida, S., 2006, “The Effect of Coolant Injection on the Endwall Flow of a High Pressure Turbine,” ASME Turbo Expo, Barcelona, Spain, May 8–11, ASME Paper No. GT2006-91060.
- [6] Paniagua, G., Denos, R., and Almeida, S., 2004, “Effect of the Hub Endwall Cavity Flow on the Flow-Field of a Transonic High-Pressure Turbine,” *ASME J. Turbomach.*, **126**(4), pp. 578–586.
- [7] Reid, K., Denton, J., Pullan, G., Curtis, E., and Longley, J., 2006, “The Effect of Stator–Rotor Hub Sealing Flow on the Mainstream Aerodynamics of a Turbine,” ASME Turbo Expo, Barcelona, Spain, May 8–11, ASME Paper No. GT2006-90838.
- [8] Marini, R., and Girgis, S., 2007, “The Effect of Blade Leading Edge Platform Shape on Upstream Disk Cavity to Mainstream Flow Interaction of a High-Pressure Turbine Stage,” ASME Turbo Expo, Montreal, Canada, May 14–17, ASME Paper No. GT2007-27429.
- [9] Schuepbach, P., Rose, M. G., Abhari, R. S., and Gier, J., 2011, “Influence of Rim Seal Purge Flow on the Performance of an Endwall-Profiled Axial Turbine,” *ASME J. Turbomach.*, **133**(2), p. 021001.
- [10] Binder, A., Forster, W., Mach, K., and Rogge, H., 1987, “Unsteady Flow Interaction Caused by Stator Secondary Vortices in a Turbine Rotor,” *ASME J. Turbomach.*, **109**(2), pp. 251–257.
- [11] Chaluvadi, V. S. P., Kalfas, A. I., and Hodson, H. P., 2004, “Vortex Transport and Blade Interactions in High Pressure Turbines,” *ASME J. Turbomach.*, **126**(3), pp. 395–406.
- [12] Matsunuma, T., 2007, “Unsteady Flow Field of an Axial-Flow Turbine Rotor at a Low Reynolds Number,” *ASME J. Turbomach.*, **129**(2), pp. 360–371.
- [13] Ch. Kasper, M.G., Rose, S. S., and Gier, J., 2008, “A Study of Unsteady Secondary Flow in a Water Flow Axial Turbine Model,” ASME Turbo Expo, Berlin, June 9–13, ASME Paper No. GT2008-50239.
- [14] Jenny, P., Abhari, R. S., Rose, M. G., Brettschneider, M., and Gier, J., 2011, “A Low Pressure Turbine With Profiled End Walls and Purge Flow Operating With a Pressure Side Bubble,” *ASME J. Turbomach.*, **134**(6), p. 061038.
- [15] Kupferschmied, P., Kopperl, O., Gizzi, W. P., and Gyarmathy, G., 2000, “Time Resolved Flow Measurements With Fast Aerodynamic Probes in Turbomachinery,” *Meas. Sci. Technol.*, **11**, pp. 1036–1054.
- [16] Pfau, A., Schlienger, J., Kalfas, A. I., and Abhari, R. S., 2003, “Unsteady 3-Dimensional Flow Measurement Using a Miniature Virtual 4-Sensor Fast Response Aerodynamic Probe (FRAP),” ASME Turbo Expo, Atlanta, GA, June 16–19, ASME Paper No. GT2003-38128.
- [17] Mansour, M., Chokani, N., Kalfas, A. I., and Abhari, R. S., 2008, “Time-Resolved Entropy Measurements Using a Fast Response Entropy Probe,” *Meas. Sci. Technol.*, **19**(11), p. 115401.
- [18] Bashforth, F., and Adams, J., 1883, *An Attempt to Test the Theories of Capillary Action by Comparing the Theoretical and Measured Forms of Drops of Fluid, With an Explanation of the Method of Integration Employed in Constructing the Tables Which Give the Theoretical Forms of Such Drops*, Cambridge University Press, Cambridge, MA.
- [19] Schuepbach, P., Rose, M. G., Abhari, R. S., Germain, T., Raab, I., and Gier, J., 2010, “Effects of Suction and Injection Purge-Flow on the Secondary Flow Structures of a High-Work Turbine,” *ASME J. Turbomach.*, **132**(2), p. 021021.
- [20] Schuepbach, P., Rose, M. G., Abhari, R. S., Germain, T., Raab, I., and Gier, J., 2008, “Improving Efficiency of a High-Work Turbine Using Non-Axisymmetric Endwalls. Part II—Time-Resolved Flow Physics,” ASME Turbo Expo, Berlin, June 9–13, ASME Paper No. GT2008-50470.
- [21] Moore, J., 1973, “A Wake and an Eddy in a Rotating, Radial-Flow Passage—Part 1: Experimental Observations,” *ASME J. Eng. Power*, **95**(3), pp. 205–212.
- [22] Greitzer, E. M., Tan, C., and Graf, M., 2004, *Internal Flow, Concepts and Applications*, 1st ed., Cambridge University Press, Cambridge, MA.